

Silicon nanostructures for photonics

**P Bettotti, M Cazzanelli, L Dal Negro, B Danese, Z Gaburro, C J Oton,
G Vijaya Prakash and L Pavesi**

INFN and Dipartimento di Fisica, Università di Trento, via Sommarive 14, 38050 Povo Trento,
Italy

Received 18 December 2001, in final form 4 March 2002

Published 22 August 2002

Online at stacks.iop.org/JPhysCM/14/8253

Abstract

Nanostructuring silicon is an effective way to turn silicon into a photonic material. In fact, low-dimensional silicon shows light amplification characteristics, non-linear optical effects, photon confinement in both one and two dimensions, photon trapping with evidence of light localization, and gas-sensing properties.

(Some figures in this article are in colour only in the electronic version)

1. Introduction

Silicon (Si) is the leading material as regards high-density electronic functionality. Integration and economy of scale are the two key ingredients in the technological success of Si. Its band gap (1.12 eV) is ideal for room temperature operation, and its oxide (SiO₂) allows the processing flexibility to place more than 10⁸ transistors on a single chip. The continuous improvements in Si technology have made it possible to grow and process 300 mm wide single Si crystals at low cost and even larger crystals are now under development. The high integration levels reached by the Si microelectronic industry in the nanometre range have permitted a whole electronic system to be included on a single chip (the system-on-chip (SoC) approach). This yields incredible processing capability and high-speed device performance. However, all single transistors and electronic devices have to transfer information on length scales which are very long compared to their nanometre scale. Lengths of 15 km in a single chip are today common, while in ten years these will reach more than 91 km [1]. This degree of interconnection is sufficient to cause significant propagation delays, overheating, and information latency. Overcoming this interconnection bottleneck is one of the main motivations and opportunities for present-day Si-based microphotonics [2]. Microphotonics attempts to combine photonic and electronic components on a single Si chip. Both hybrid and monolithic approaches are possible. Replacement of electrical with optical interconnects has appealing potentialities, such as higher-speed performance and immunity to signal cross-talk.

The development of Si-based photonics has lagged far behind the development of electronics for a long time. The main reason for this slow progress has been the lack of

practical Si light sources, i.e., efficient Si light-emitting diodes (LED) and injection lasers. Si is an indirect-band-gap material. Light emission in indirect materials is naturally a phonon-mediated process with low probability (spontaneous recombination lifetimes in the millisecond range). In standard bulk Si, competitive non-radiative recombination rates are much higher than the radiative ones and most of the excited e–h pairs recombine non-radiatively. This yields very low internal quantum efficiency ($\eta_i \approx 10^{-6}$) for Si luminescence. As regards the lasing of Si, fast non-radiative processes such as Auger or free-carrier absorption strongly prevent population inversion at the high pumping rates needed to achieve optical amplification. However, during the last ten years, many different strategies have been employed to overcome these material limitations. Present-day Si LED are only a factor of ten away from the market requirements [3, 4] and optical gain has been demonstrated [5].

Availability of Si nanotechnology played a primary role in these achievements. Today we know that in Si nanocrystals (Si-nc) the electronic states—as compared to bulk Si—are dramatically influenced both by quantum confinement (QC) and by the enhanced role of states—and defects—at the surface. The effect of QC is a rearrangement of the density of electronic states in energy as direct consequence of volume shrinking in one, two, or even three dimensions, which can be obtained, respectively, in quantum wells, wires, and dots. On the other hand, the arrangement of the atomic bonds at the surface also strongly affects the energy distribution of electronic states, since in Si-nc the Si atoms are either at the surface or a few lattice sites away. The QC and a suitable arrangement of interfacial atomic bonds can provide in Si-nc radiative recombination efficiencies that are orders of magnitude larger than in bulk Si, significant optical non-linearity, and even optical gain [5].

The aim of this work is to review our recent accomplishments in the field of silicon photonic, reporting some unpublished data too, and to compare them with the state of the art in the field. For this reason, some Si-nc growth techniques are discussed. We focus on porous silicon (PS) [6], ion-implanted Si [7], and plasma-enhanced chemical vapour deposition (PECVD) [8], since it is our aim to discuss in detail some interesting optical properties observed in these materials. However, other techniques are also known, such as laser ablation [9], molecular beam epitaxy [10], sputtering [11], and gas evaporation [12].

PS occupies a special place, since it was the first—and it is still the least expensive—material using which the optical properties of Si-nc have been studied. Efficient room temperature visible emission was observed in PS in 1990 [13], although PS was already known [14]. Nanocrystalline PS is a sponge-like structure with features (i.e. pores and undulating wires) with sizes of the order of a few nm, obtained most commonly by electrochemical anodization using HF-based solution [6].

The fabrication procedure for PS is very flexible. In fact, PS can be fabricated also in multilayer structures and bi-dimensional arrays of so-called macropores, i.e. straight tubular holes with extraordinary aspect ratios (circular sections with radii of the order of a μm , and lengths of several tens or even hundreds of μm). Both multilayers [15] and macroporous Si [16] have provided a cheap way to fabricate large structures with, respectively, one- and two-dimensional periodicity in the dielectric properties. Such structures can present photonic band gaps (PBG) [17]. In PBG materials, the index of refraction is a periodic function of space, so the photon dispersion curve folds and forms energy bands, Brillouin zones, and in particular energy band gaps for photons. The phenomenon is much the same as for electrons in crystals, where the electrical potential is periodic in space. For this reason PBG materials are also called photonic crystals (PC).

With the possibility of growing several tens and even hundreds of different PS layers on top of each other, aperiodic PS multilayer structures provide also a convenient way to study the effects of disorder on the propagation of light [18]. We are interested in using aperiodic

PS multilayers to look for one such effect, which is Anderson localization, first predicted for electronic states in disordered potential distributions [19]. Anderson localization of photons occurs in the so-called strong-scattering regime, when the scattering mean free path of photons, i.e. the average distance that the wave can travel between two successive scattering events, becomes smaller than some critical value. In such a regime, the photon diffusion constant is found to vanish. Moreover, the field intensity in localized regions can be significantly larger than in the surroundings. Localization of a strong electromagnetic field inside limited Si volumes can have interesting applications, such as achievement of non-linear optical effects at low power.

This paper is organized in the following way. Section 2 introduces the methods used to fabricate silicon nanocrystals. Section 3 discusses their optical properties. Linear as well as non-linear optical properties are presented. Section 4 reports on gain measurements on silicon nanocrystals with a discussion of the models proposed to explain population inversion. Section 5 is a review of the existing strategies for obtaining a silicon laser. Section 6 refers to PS and to its photonic applications. Microcavities, multiparametric gas sensors, LED, PC, and Fibonacci quasicrystals for Anderson localization studies are all presented. Section 7 concludes the paper by putting these results into perspective and considering future possibilities.

2. Fabrication of Si nanocrystals

2.1. Porous Si

PS is formed by electrochemical anodization of Si in an HF electrolyte. The solution employed is typically aqueous 50% HF mixed with ethanol. The electrical source chosen for the process is usually current controlled, because the current density and the porosity are directly related. The anodization reaction at the Si/electrolyte interface requires the presence of holes [20]. Therefore, the natural choice for substrate doping is p-type. However, n-type substrates can also be employed for PS fabrication, provided that generation mechanisms for excess holes are available—for example, by using light beams, or by biasing the substrate in the breakdown regime. PS fabricated on lightly p-type-doped substrates has an average nanocrystal size of about 2–5 nm. Since the exciton Bohr radius in Si is around 4.3 nm, QC effects—and in particular, large values of photoluminescence (PL) efficiency—are especially evident in this type of PS. On the other hand, in highly p-type-doped wafers (i.e., with typical resistivity values around 0.01 Ω cm), the size of the pores and structures is of the order of 10 nm. The QC effects are in this case less important, thus explaining why the PL emission is remarkably more weak in low-resistivity PS. However, carrier transport can be tuned over a much wider range, and larger porosity ranges can be obtained.

In order to finely tune the structural and optical properties of PS layers, it is necessary to know the etch rate and the porosity of the layer, as functions of doping level, anodization current density, and composition of the electrolyte. The etch rate is relevant to control of the layer thickness. The porosity (the fraction of Si removed from the substrate) is relevant for two reasons. On one hand, the structure size depends on the porosity. On the other hand, the value of the porosity is directly linked to the effective index of refraction of the PS layers. Indeed, as long as the typical structure size is much lower than the emission wavelength, the PS layers appear as an effective medium, whose index of refraction has an intermediate value between the index of refraction of Si (structures) and that of the air (pores). The weight of the pore contribution is precisely the porosity. Several estimation procedures have been suggested for evaluating the effective dielectric constant ϵ_{eff} of PS layers. For example, a commonly

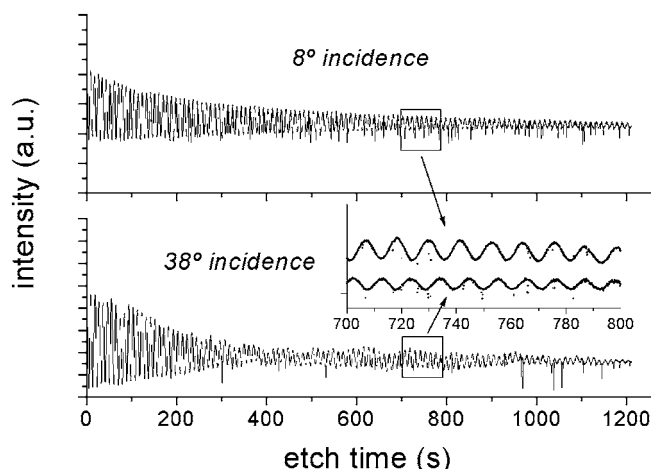


Figure 1. Intensity of reflected beams versus time during anodization. The sporadic spikes are due to bubbles which caused deviation or scattering of the laser beams.

used one is the Bruggeman effective medium theory, in which the porosity and the dielectric constant are related by the following formula [15, 21]:

$$f \frac{\varepsilon - \varepsilon_{eff}}{\varepsilon + 2\varepsilon_{eff}} + (1 - f) \frac{\varepsilon_M - \varepsilon_{eff}}{\varepsilon_M + 2\varepsilon_{eff}} = 0 \quad (1)$$

where f is the volumetric fraction of Si—so the porosity φ is $(1 - f)$ —and ε , ε_M are the dielectric functions of Si and of the embedding medium (air). With this formula, ε_{eff} can be calculated.

It is usually assumed that the dissolution of Si only takes place at the pore tips, which means that the etching of a thicker layer does not affect the porous film already etched. This assumption is fairly reasonable, as experimentally demonstrated, and convenient, due to the difficulty in measuring deviations from constant etch rates. However, the porosity is not homogeneous in depth [22–25]. The amounts of these deviations from constant etch rate and constant porosity represent a critical issue for optical devices based on interference between stacked PS layers. To measure these deviations accurately, *in situ* techniques can be employed. If a laser beam is pointed at the growing layer, interference fringes can be observed in reflectance [26]. The interference is between the beams reflected at the PS/electrolyte and at the PS/substrate interfaces. As the PS/substrate interface moves during the etch, the reflectivity signal oscillates in time. The frequency of the oscillations yields the optical path (nd) of the layer etched per unit time. To measure the refractive index and the etch rate independently, two beams with different angles must be analysed. Measuring the frequencies of both signals, the index profile of the layer and the etch rate evolution can be calculated [27]. In figure 1 we shown the interference patterns observed for two different angles, and figure 2 shows the estimated layer inhomogeneity. Another appealing peculiarity of this technique is that it provides the possibility of running a complete characterization of etch rate and porosity versus etching current density using one single sample. This is performed by sweeping the range of currents desired and measuring the frequencies of the interference signals with respect to the current. Figure 3 shows this dependence for a 13% HF solution for one single sample with $0.01 \Omega \text{ cm}$ of resistivity.

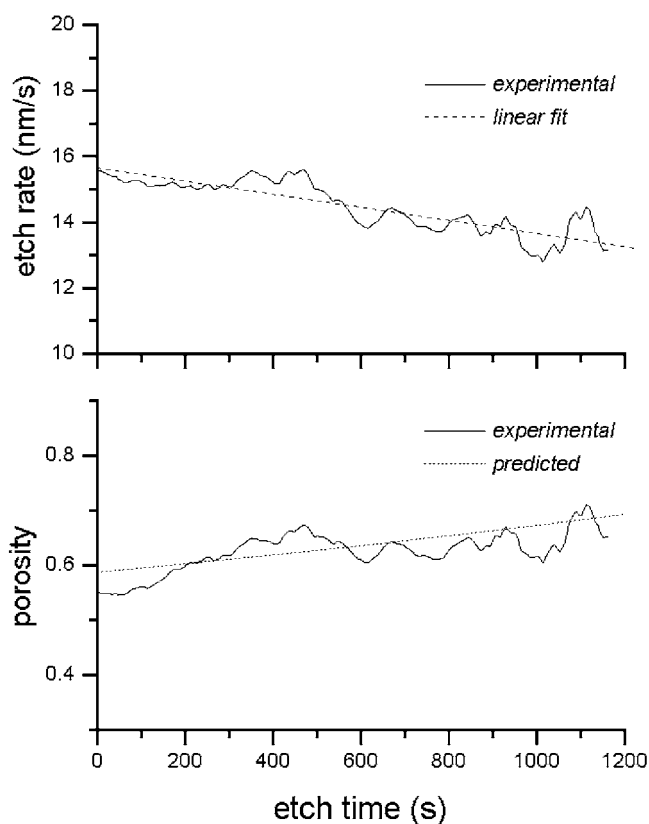


Figure 2. Etch rate and porosity evolution, from the data of figure 1. The top plot shows the etch rate versus time (solid curve) and its linear fit (dashed line). The bottom plot shows porosity versus time directly extracted from experimental data (solid curve), and porosity calculated from the linear fit of the etch rate and a constant-valence approximation (dotted line).

2.2. Ion-implanted Si nanocrystals

As the internal surface of PS is enormous, it is also very reactive. This makes PS very interesting for sensor applications but it is a problem when PS is used in photonic devices. Thus alternative techniques have been developed to produce Si-nc. Ion-implanted Si-nc can be obtained by implanting Si into Si wafers or SiO₂ substrates (quartz or thermally grown oxide) and by annealing the samples. In contrast to PS, implanted Si-nc are very stable and form a reproducible system fully compatible with VLSI technology. The presence of a high-quality SiO₂ matrix guarantees superior O passivation of Si-related dangling bonds and non-radiative centres. In addition, the interface between the Si-nc surface and the SiO₂ matrix can play an active and crucial role in the radiative recombination mechanism.

For optical gain measurements, Si-nc have been produced in Catania (Italy) by the group of F Priolo by ion implantation ($80 \text{ keV} - 1 \times 10^{17} \text{ Si cm}^{-2}$), followed by high-temperature thermal annealing ($1100 \text{ }^\circ\text{C} - 1 \text{ h}$). Quartz wafers were used for optical transmission experiments. Transmission electron microscopy (TEM) of these samples showed the presence of Si-nc embedded within the oxide matrix, at a depth of 110 nm from the sample surface and extending over a thickness of 100 nm. Their diameters were $\sim 3 \text{ nm}$ and the Si-nc concentration was $\sim 2 \times 10^{19} \text{ cm}^{-3}$.

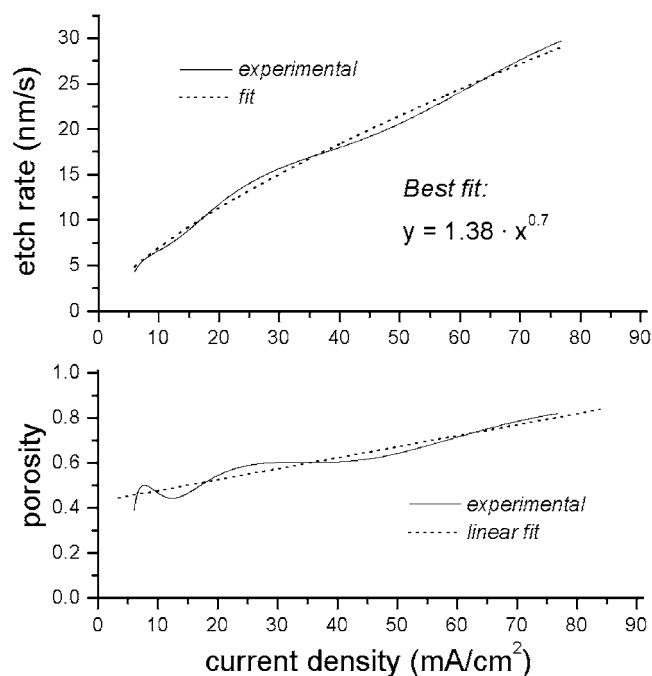


Figure 3. Etch rate and porosity curves versus current density measured on one single sample.

The structure of these samples where a layer of Si-nc is buried in a SiO₂ matrix forms a planar dielectric waveguide. The Si-nc implanted region has an effective refractive index n larger than that of SiO₂. It is possible to estimate the effective refractive index n of the core region by using equation (1), which yields $n = \sqrt{\epsilon_{eff}} = 1.89$ for a volumetric fraction $f = 0.28$. The waveguide structure can sustain a mode at 0.8 μm with a confinement factor (ratio of the optical mode in the Si-nc region versus the total mode extent) of 0.097.

2.3. PECVD-grown Si nanocrystals

Si-nc can be also formed by high-temperature annealing of substoichiometric SiO₂ thin films deposited by PECVD. In this technique, the desired flow ratio of the high-purity source gases SiH₄ and N₂O is controlled to produce excess Si content in substoichiometric SiO₂ thin films at a pressure of 10⁻² Torr. After the deposition, the SiO_x films are annealed at high temperatures under a nitrogen atmosphere. Thermal annealing of the SiO_x films leads to the separation of the SiO_x phase into Si and SiO₂, and Si-nc embedded in a SiO₂ matrix are formed (see figure 4). The samples discussed here have been produced by F Iacona at IMETEM-CNR in Catania (Italy).

3. Optical properties of Si nanocrystals

3.1. Photoluminescence

According to their surface termination, Si-nc can be classified into two categories: hydrogen or oxygen terminated. Nanocrystals of freshly prepared PS belong to the first category, whereas the later category contains aged and oxidized-surface PS and Si-nc embedded in SiO₂ thin

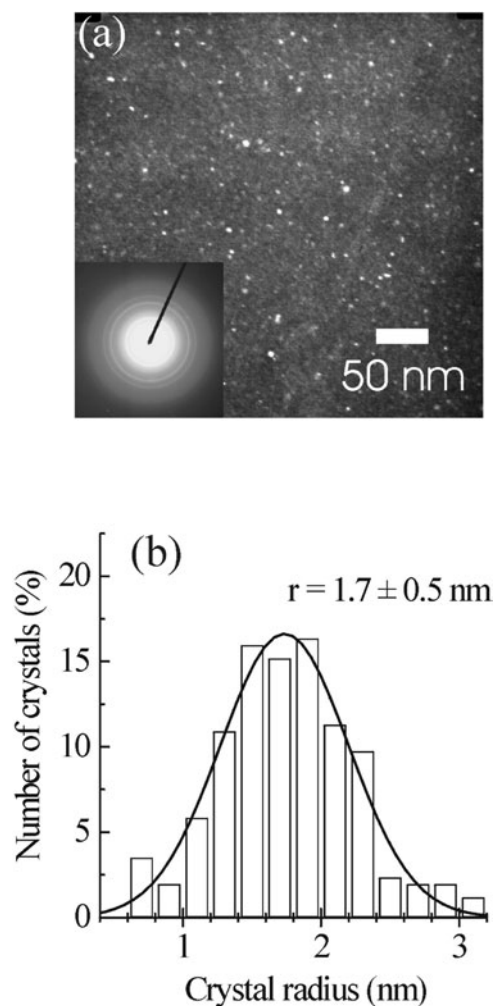


Figure 4. (a) A plan-view TEM micrograph and (b) the relative Si-nc size distribution for SiO_x film formed by PECVD for a Si concentration of 42 at.% after annealing at 1250 °C. The electron diffraction pattern for this sample is also reported, in the inset in (a) [8]. Courtesy of F. Iacono CNR-IMETEM.

films. For H-terminated PS, PL spectra show a continuous shift of peak energy from the bulk band gap to the visible region with a good agreement with the QC effect, whereas the PL spectra of oxidized-surface PS are confined to a specific region.

Although PL has been studied in depth for PS, it is interesting to consider common features that can be found also in Si-nc grown by different methods. It is established that Si-nc exhibit strong PL in the red region and progressively shift towards the blue when the mean size decreases [28]. Similarly, the edge of the absorption spectra also shifts towards the blue with decrease of the Si-nc size. However, a quantitative discrepancy between the energy of PL and the optical band gap calculated from the QC theory exists. Suggested models of the PL mechanism include the QC model, which proposes that the QC raises the band gap and the PL originates from transitions between the band edges, and the interface state model, where carriers are first excited within the Si-nc, then relax into interface states and recombine

radiatively there. Other suggestions involve chemical defects induced at the preparation level such as P_b centres [29–33].

While the oxygen passivation is considered to strengthen the PL emission [34], such passivation induces some defects, which appears as a blue band beside the Si-nc emission [35]. One of the defects is due to Si dangling bonds at the interface between the Si and SiO_2 (P_b centre) that act as non-radiative recombination centres, thereby decreasing the band-edge emission efficiency [36]. An improvement in the PL emission of Si-nc is achieved by using phosphosilicate glass instead of pure SiO_2 as the surrounding matrix for Si-nc. In this way, the PL increases with the P (in the form of P_2O_5) concentration while the P_b -centre-related emission decreases [37].

In PECVD-grown Si-nc, a strong correlation has been observed between the Si-nc size and the PL data. It apparently suggests that the light emission from the Si-nc is due to band-to-band radiative recombination of electrons–hole pairs confined within the nanocrystals. However, a deviation is observed between the observed PL data and the theoretical calculations for the fundamental band gap based on the QC theory. In such cases, a mixed model explains the experimental results well; in this model the light emission originates from the radiative recombination process at radiative interface states inside the band gap and the corresponding Si/ SiO_2 interface states. The energy levels of these states are not fixed, like in the case of other luminescent defects, but strongly depend on the size of the nanocrystals [8, 28, 29].

3.2. Nonlinear optical properties of Si nanocrystals

Besides the linear optical properties, non-linear optical properties are also of major interest for photonic device applications such as in all-optical switching. Intensity-dependent changes in the optical properties are prominent at high intensities (I) of the pump laser, particularly third-order non-linear effects. Enhanced optical non-linearity has been reported for PS at different wavelengths [38, 39]. Very few reports are available on other kinds of Si-nc and they are prepared by sol–gel, laser ablation, ion implantation, and PEVCD techniques [40–43].

Third-order non-linear effects are generally characterized by the non-linear absorption (β) and the non-linear refractive index (γ). The non-linear coefficients, namely β and γ , are described by $\alpha(I) = \alpha_0 + \beta I$ and $n(I) = n_0 + \gamma I$ where α_0 and n_0 stand for the linear absorption and refractive index respectively. The β - and γ -values are used to evaluate the imaginary ($\text{Im } \chi^{(3)}$) and real ($\text{Re } \chi^{(3)}$) parts of the third-order non-linear susceptibility. One of the most versatile techniques for measuring $\text{Im } \chi^{(3)}$ and $\text{Re } \chi^{(3)}$ is the single-beam technique, referred to as z -scanning [43, 44]. Measuring the transmission (with and without an aperture in the far field) as the sample moves through the focal point of a lens (z -axis) enables the separation of the non-linear refractive index from the non-linear absorption.

3.2.1. Nonlinear refraction in Si nanocrystals. For all the samples investigated, the closed-aperture data show a distinct valley–peak configuration typical of positive non-linear effects (self-focusing), as expected for most dispersive materials [38–45]. From a fit of the z -scan curve, γ is obtained. The real part of the third-order non-linear susceptibility is obtained from $\text{Re } \chi^{(3)} = 2n^2 \varepsilon_0 c \gamma$, where n is the linear refractive index, ε_0 is the permittivity of free space, c is the velocity of light. The effective refractive index, n , is considered to be 1.7, obtained from independent measurements on these samples. For the measurements shown in figure 5 (top plot), $\text{Re } \chi^{(3)} = (1.3 \pm 0.2) \times 10^{-9}$ esu.

3.2.2. Nonlinear absorption in Si nanocrystals. Figure 5 (bottom plot) shows the normalized open-aperture transmission (full power into the detector) as a function of z for a PECVD-grown

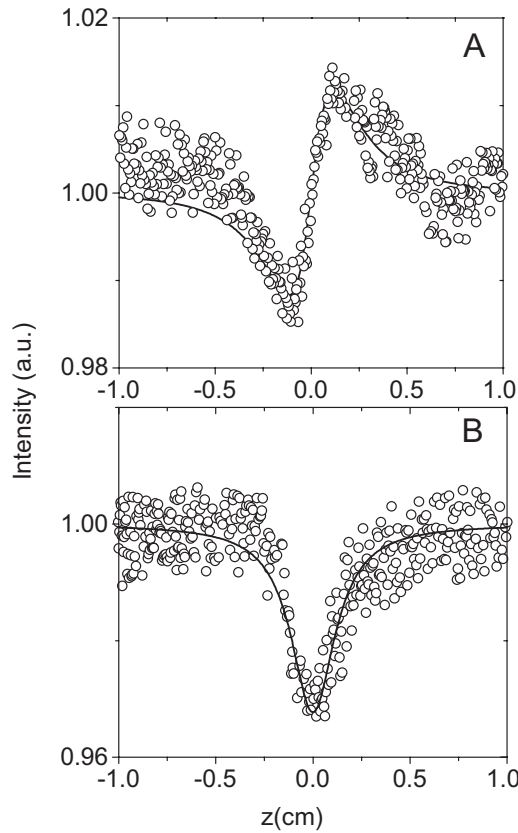


Figure 5. (a) A closed-aperture z -scan for Si-nc grown by PECVD ($\lambda = 800$ nm, pulse width 60 fs) for Si concentration 42 at.%, annealed at 1250 °C. (b) An open-aperture z -scan for 39 at.%, annealed at 1200 °C [43].

sample. A symmetric inverted-bell-shaped transmission is measured with a minimum at the focus ($z = 0$). When direct absorption is negligible, one can deduce the non-linear absorption coefficient, β , from the open-aperture z -scan data. For a thin sample of thickness l [40]:

$$T(z) = 1 + \frac{\beta I_0 l}{(1 + z^2/z_0^2)}. \quad (2)$$

The open-aperture experiment is carried out several times and for different peak intensities between 0.3 and $2 \times 10^{10} \text{ W cm}^{-2}$ to ensure that proper measurements have been made. The measured β -values for Si-nc are higher than the values for crystalline silicon (c-Si) [46, 47] and close to the values for PS [38]. The present values are enhanced by two orders of magnitude over the theoretically predicted non-linear absorption coefficients for c-Si [47]. Knowing β , the imaginary part of the third-order non-linear susceptibility $\chi^{(3)}$ is evaluated from $\text{Im } \chi^{(3)} = n^2 \epsilon_0 c \lambda \beta / 2\pi = (0.6 \pm 0.09) \times 10^{-10} \text{ esu}$.

The non-linear absorption in most of the refractive materials arises from either direct multiphoton absorption or saturation of single-photon absorption [44]. z -scan traces with no aperture are expected to be symmetric with respect to the focus ($z = 0$) where they have the minimum transmittance (for two-photon or multiphoton absorption) or maximum transmittance (for saturation of absorption). It is interesting to note that the non-linear absorption in Si-nc

formed by ion implantation and laser ablation is selective as regards the excitation as well as cluster size [40,41,48,49]. For example, laser-ablated samples exhibit saturation of absorption and bleaching effects (change of sign of the non-linear absorption from positive to negative with the increase of the pump intensity) at near-resonant excitations (355 and 532 nm) [48]. In contrast, ion-implanted samples show an almost linear dependence of β on the pump power, clear evidence of two-photon non-linear processes [49]. Here, we observe neither saturation nor bleaching of absorption. Indeed the absorption at 813 nm is extremely weak or even negligible [28]. In addition, the laser energy ($\hbar\omega$) that we used meets the two-photon absorption (TPA) condition [50], $E_{g2} < 2\hbar\omega < 2E_{g2}$, where E_{g2} is the optical band gap [28]. Figure 5 (bottom plot) shows a well-defined bell-shaped minimum transmittance at the focus. All of these features suggest TPA as the origin of the non-linear absorption.

3.2.3. Size correlation with non-linear coefficients in Si nanocrystals. By comparing $\text{Re } \chi^{(3)}$ and $\text{Im } \chi^{(3)}$ one can conclude that $\text{Re } \chi^{(3)} \gg \text{Im } \chi^{(3)}$ —that is, the non-linearity is mostly refractive. The absolute values of $\chi^{(3)} = ((\text{Re } \chi^{(3)})^2 + (\text{Im } \chi^{(3)})^2)^{1/2}$ are significantly larger than the bulk Si values ($\sim 6 \times 10^{-12}$ esu) [47, 51] and are of the same orders of magnitude as those reported for PS [38] and for glasses containing nanocrystallites [45, 52]. The increase of $\chi^{(3)}$ with respect to bulk values in low-dimensional semiconductor is attributed to several mechanisms [53–57]. Among them, only the intraband transitions are expected to be size dependent, as they originated from modified electronic transitions by the QC effects [53]. Hence the $\chi^{(3)}$ -increase is mainly due to QC.

QC effects on $\chi^{(3)}$ have been estimated in several works [54–58]. Theoretical attempts were made to study PS as a one-dimensional quantum wire and for non-resonant excitation conditions [54, 58]. It was found that the increase in the oscillator strengths caused by the confinement-induced localization of excitons gives rise to the increase of $\chi^{(3)}$. In fact, the exciton Bohr radius a_0 decreases with the size of quantum wires with respect to the bulk value and hence $\chi^{(3)}$ sensitively increases proportionally to $1/a_0^6$. The estimated $\chi^{(3)}$ for PS is close to the value for PS measured in [54] and slightly larger than what we measured and other reported values [38]. The dependence of $\chi^{(3)}$ on Si-nc radius (r) is plotted in figure 6. The increase in $\chi^{(3)}$ is not as sharp as expected from the theoretical model, but follows more closely $\chi_{\text{Si-nc}}^{(3)} = \chi_{\text{bulk}}^{(3)} + A/r + B/r^2$. A similar polynomial dependence is expected theoretically for the size dependence of the emission energies of Si-nc [28]. In reality, the experimentally determined $\chi^{(3)}$ is related to the microscopic $\chi_m^{(3)}$ by $\chi^{(3)} = p|f|^4\chi_m^{(3)}$, where p is the volume fraction and f is a local field correction that depends on the dielectric constant of the embedded matrix and nanocrystals [53]. Hence, in addition to r , other parameters such as the effective refractive index and volume fraction of Si-nc in the embedded matrix are to be taken into account [56]. This could explain the scatter in the data of figure 6.

4. Optical gain in ion-implanted Si nanocrystals

We have reported on single-pass gain in pump-and-probe transmission experiments on ion-implanted Si-nc in quartz substrates [59]. We claim that population inversion is possible between the fundamental and radiative Si=O interface states. This model explains the gain and accounts for the lack of Auger saturation and free-carrier absorption. We found that the critical issues as regards obtaining sizable gain are (1) high oxide quality, (2) high areal density of Si nanocrystals, and (3) appropriate waveguide geometry of the Si-nc samples.

The gain coefficient was measured by the variable-strip-length (VSL) method where the amplified spontaneous emission intensity emitted from the sample edge is collected as

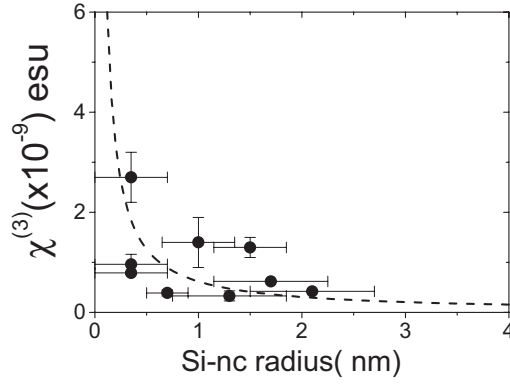


Figure 6. The variation of $\chi^{(3)}$ with the Si-nc radius (r) in Si-nc grown by PECVD. The inset shows the PL peak maxima variation with the Si-nc radius. The dashed curves show the fit to a $\chi_{\text{Si-nc}}^{(3)} = \chi_{\text{bulk}}^{(3)} + A/r + B/r^2$ dependence [43].

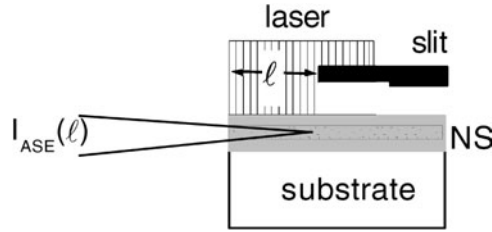


Figure 7. A sketch of the variable-strip-length method. The amplified luminescence intensity from the sample edge is recorded as a function of the slit width ℓ .

a function of a linear excitation volume [60]. The VSL method is based on the measurement of the luminescence emitted from the sample edge as a function of the linear dimensions of the excited region (ℓ ; see figure 7). From a fit of the resulting curve, the optical gain g can be deduced at every wavelength. By assuming a one-dimensional amplifier model, I_{ASE} can be related to g by [60, 61]

$$I_{ASE}(\ell) \propto \frac{I_{SPONT}}{g - \alpha} (e^{(g-\alpha)\ell} - 1), \quad (3)$$

where I_{SPONT} is the spontaneous emission intensity and α an overall loss coefficient. The gain measured in this way is the modal gain, the material gain weighted by the optical confinement factor of the guided mode [62]. The spectral dependence of the net modal gain can be derived by using [60, 61]

$$g = \frac{1}{\ell} \left[\ln \left(\frac{I_{ASE}(\ell)}{I_{ASE}(2\ell)} - 1 \right) \right] \quad (4)$$

where the ratio of the luminescence spectrum at a length ℓ is divided by the luminescence spectrum at a length 2ℓ . Care has to be taken to ensure that these lengths are within the exponentially rising part of the gain curve.

Exponential increase in the emitted intensity, line narrowing, and directionality of the stimulated emission have been previously reported [59]. In figure 8, some recent VSL results obtained with high-intensity visible excitation on a transparent sample are shown. The VSL curves of figure 8 have been measured using an intense CW argon laser at an average power of

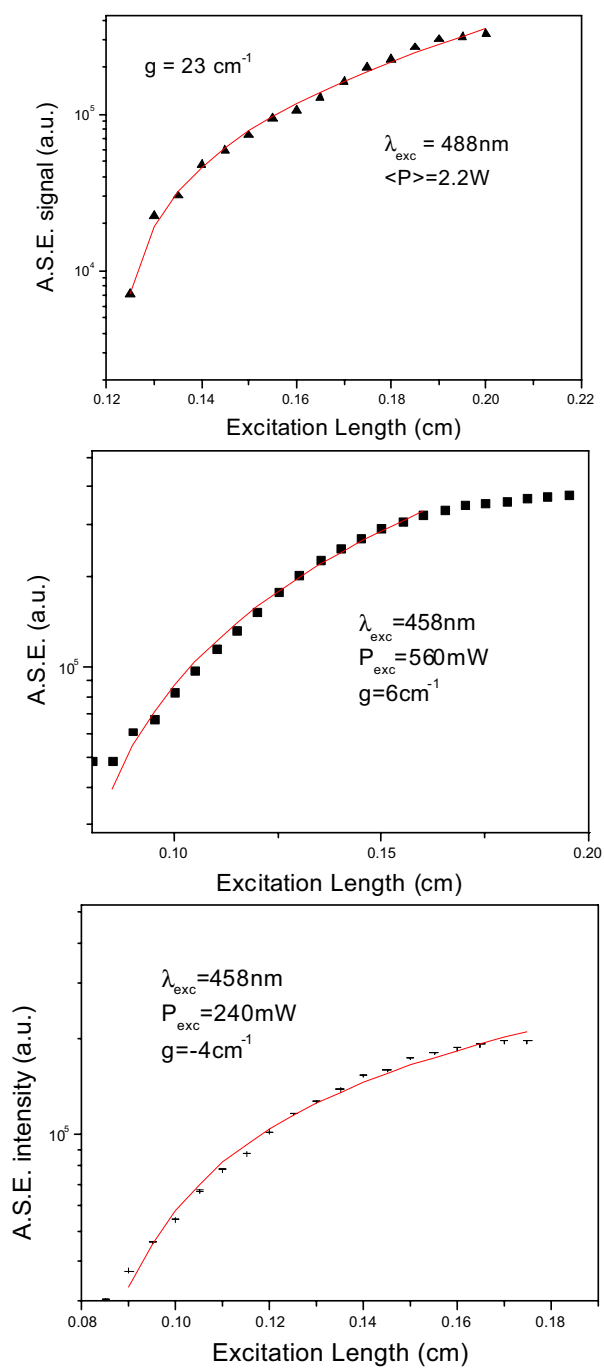


Figure 8. Top: the VSL curve for a sample of kind A (transparent, on quartz) obtained with the visible 488 nm excitation line for an average power of 2.2 W. The detection wavelength is 750 nm. Middle: the VSL curve for a sample of kind A (transparent, on quartz) obtained with the visible 458 nm excitation line for an average power of 560 mW. The detection wavelength is 750 nm. Bottom: the VSL curve for a sample of kind A (transparent, on quartz) obtained with the visible 458 nm excitation line for an average power of 240 mW. The detection wavelength is 750 nm.

2.2 W (corresponding to an intensity of 20 kW cm^{-2}) measured on the sample. The measured modal gain coefficient obtained from the best fit with the linear amplifier model [63] yields a value of $g = 23 \text{ cm}^{-1}$. The ℓ -range shown in figure 8 is the region where the laser excitation has a homogeneous intensity profile and where the light coupling with the physical edge of the sample is free from diffraction artifacts. VSL results are also reported here for the 458 nm excitation at intermediate power. At an average power of 560 mW we measured an optical gain of just 6 cm^{-1} , while on decreasing the pump power to 240 mW we measured optical losses of -4 cm^{-1} , according with the reduced pumping power. The measured gain values reported in the current work are smaller than the values reported in [59] because of the reduced absorption coefficient of our structures in the visible part of the spectrum. An additional limiting factor is the effectively reduced pumping photon flux when visible light instead of UV light is used.

To build a model to help us to understand the gain data, we considered two facts:

- (a) in the literature there exist some proofs that Si and other Si-based systems do not show any optical gain for interband transitions due to the presence of a strong free-carrier absorption, which prevents the population inversion and of fast Auger relaxation processes [64];
- (b) a great amount of evidence suggests that the 750–800 nm near-infrared emission band is due to radiative Si/O interface states.

From these, a three-level model naturally emerges and explains the gain. Several papers report on the existence of interface states in Si nanocrystals [65] which can trap electrons, and recently more sophisticated models appeared such as the Si–Si dimer [66] and the self-trapped exciton [67]. Here we do not want to discuss the microscopic picture of these interface states, but simply suggest that in our system the photoexcited electrons are mainly trapped into these interface states from where they recombine radiatively. It is exactly this transition (an electron from the interface state to a hole in the valence band) which allows gain in our system. The localized nature of the inverted state prevents there being a significant role for free-carrier absorption, because carriers in these states are no longer free, but confined. Further experimental evidence, i.e. low absorption cross sections at 750 nm and fast recombination dynamics, suggests that a four-level model would be more appropriate. The four levels could be due to the conduction and valence Si-nc states and an internal transition of the interface states. Indeed, the details of the gain model are still under debate. Here, what we want to stress is the critical role played by the interface states.

5. Si lasers

The experimental results reported in the previous section open the way to research towards a silicon laser. Indeed, a popular magazine entitled a review on this ‘The race is open towards the silicon laser’. It is thus worth trying to summarize the principal alternative results that have been published.

5.1. Doping of Si with rare earths

Rare-earth-doped Si-nc provides one of the most promising routes towards a Si laser [68]. In this system, luminescence is due to an internal 4f shell transition of rare-earth ions excited via excitons generated in Si. Among other systems, erbium (Er) is the most interesting, since it emits light at $1.54 \mu\text{m}$ where optical fibres have a transparency window. Initial problems concerning the Er incorporation and the luminescence quenching in bulk Si have now been fully understood. The most important limiting effects concern the presence of fast non-radiative decay channels such as energy back-transfer (the energy is transferred back from excited Er ions to electron–hole pairs) and Auger relaxation processes (the energy is released to free

carriers) [69, 70]. Nevertheless, light-emitting devices operating at room temperature with efficiencies of 0.1% and modulation speed of 10 MHz have already been demonstrated [71, 72]. Since Er ions in SiO₂ have a relatively low gain, the gain in Si codoped with Er and O is expected to be even lower. For this reason, low-threshold laser resonator structures have been proposed which include mushroom-shaped Si:Er microdisc Si-on-insulator (SOI) microcavities and one-dimensional photonic band-gap resonators within SOI strip channel waveguides [73].

Another very promising route relates to the strong coupling of Er ions with Si-nc [74, 75]. In fact, in a material where both Si-nc and Er ions are present, the photoexcitation is preferentially transferred from the Si-nc to the Er ions, which release it radiatively. In this way, the effective Er absorption cross section is increased by more than two orders of magnitude. Si-nc behave as sensitizers for the Er luminescence. Moreover, non-radiative de-excitation processes, such as Auger relaxation or energy back-transfer, are strongly reduced, further improving the luminescence efficiency. In this system, laser inversion could be achieved at extremely low pumping intensities [68]. Similar work has also been carried out by using PS microcavities doped with Er [76]. More details on PS in microcavities will be given in section 6.1.

5.2. Si/Ge superlattices

The QC approach towards a Si-based laser involves a variety of different structures such as multi-quantum-well (MQW) structures, superlattices (SL), and quantum dots.

A first class of lasers is based on infrared intersubband lasing transitions entirely within the valence band. A simple proposed structure is the so-called quantum parallel laser (QPL). A QPL is a Ge_{0.5}Si_{0.5}/Si superlattice made of identical square quantum wells operating at low voltage in a flat-band condition and operating at near-infrared communications wavelengths ranging from 3 to 5 μm . Gain values as high as 134 cm^{-1} for current densities of $J = 5000 \text{ A cm}^{-2}$ at room temperature have been predicted [77].

Another scheme for a Si laser capable of THz emission follows an earlier design of valence intrasubband lasers with inverted light-hole effective mass already proposed for GaAs/AlGaAs quantum wells [78]. This Si THz laser is based on the anti-crossing between heavy-hole and light-hole subbands. The SiGe/Si system is engineered to have a light-hole subband with electron-like character. The laser could be electrically pumped through resonant tunnelling in a typical quantum cascade scheme [79]. Positive optical gains ranging from 100 to 1000 cm^{-1} are predicted for tunnelling times shorter than that of the upper laser state (total population inversion), and optical gain as high as 172 cm^{-1} could be obtained even for partial (85%) population inversion between the subbands. The laser could operate at a wavelength of 50 μm but at liquid nitrogen temperature only. The most successful scheme is based on a design very similar to that of the usual III–V quantum cascade laser [80]. Electroluminescence (EL) from a LED based on this system has already been reported.

5.3. Si/SiO₂ superlattices

A claim recently appeared of finding a laser-type spectral narrowing in the EL of a Si/SiO₂ SL prepared by LP-CVD [81]. The samples consisted of four Si/SiO₂ SL where the Si thicknesses vary from 75 to 150 nm while the SiO₂ thickness was 2 nm. The EL was exceptionally non-linear for forward currents larger than 100 mA mm^{-2} . At the very same time, the original wide spectrum spanning the whole visible range collapsed into very narrow peaks (5 nm spectral width) around 650–700 nm. It is not clear whether these behaviours are due to lasing or to plasma emission in the LED. Similar reports for PS LED have been interpreted as plasma emissions.

5.4. Si nanoparticles

In addition to the data reported in section 4, evidence of population inversion and amplified spontaneous emission has been obtained for Si-nc deposited by reactive deposition onto fused quartz [82]. The luminescence decay of this Si-nc shows two typical time regimes: the usual long-lived luminescence that decays in 50 μ s and a fast luminescence at 750 nm which decays in a few ns and disappears at low pumping rates. When the VSL geometry is used, the fast luminescence is absent for short excitation lengths and follows equation (3) for increasing lengths. The interpretation was that the fast PL is due to population inversion at the Si-nc interface states with a very short lifetime for the inversion. A fast population inversion is very important for applications: it allows short light pulses to be generated.

Population inversion has been also evidenced in Si-nc reconstructed from very small (1 nm) colloidal nanoparticles [83]. Under 355 nm excitation conditions, the luminescence of such samples is dominated by naked-eye visible blue emission at 390 nm. Intense two-photon excitation at 780 nm produces blue light with a sharp threshold and non-linear power dependence up to a saturation level.

6. Porous Si devices for photonics

6.1. Microcavities

PS multilayers can be obtained by periodically varying the etch parameters, such as current density or light power, or by using periodically doped substrates [15]. The latter gives better quality structures, but the former is much more easily accomplished. Figure 9 shows an example of a Fabry–Perot structure and how simply modulating the current density causes it to grow. A Fabry–Perot structure is formed by a spacer that separates two highly reflecting distributed Bragg reflectors (DBR) [84]. Microcavities are characterized by a wavelength region where all the light is reflected (stop band) and by a resonance wavelength (λ) for which the field intensity in the cavity is enhanced. This effect dramatically narrows and strengthens the PL, which also shows strong directionality in the emission pattern [15]. An example is shown in figure 10. One problem of PS microcavities is the instability due to the aging of PS itself [85]. Aging affects mainly the PL intensity and energy. One way to prevent this effect is by oxidation of the PS microcavity which can be achieved either thermally [86] or electrochemically [87].

There are many other applications of PS multilayers apart from in DBR and microcavities. Planar waveguides can easily be achieved with PS. Waveguiding has been demonstrated experimentally both in the IR and in the visible region [88]. The main drawback of these waveguides is the loss due to scattering of the porous medium and to the absorption of PS, especially for visible applications.

6.2. Sensors

The sponge structure of PS is the cause of the high surface/volume ratio, which is typically of the order of 500 m² cm⁻³. This is responsible for the high reactivity of PS layers in contact with chemical species. This feature is an advantage if PS is exploited as a sensing material [89]. The sensing activity of PS ranges from NO₂ [90,91], to humidity [92,93], to organic molecules [89], to ethanol [94], etc. In addition, PS microcavities have been used as biosensors because of their response to DNA molecules and lipids [95], which allows the distinguishing of viral genetic chains and Gram-negative bacteria. Therefore the fields of application of PS sensors are very varied.

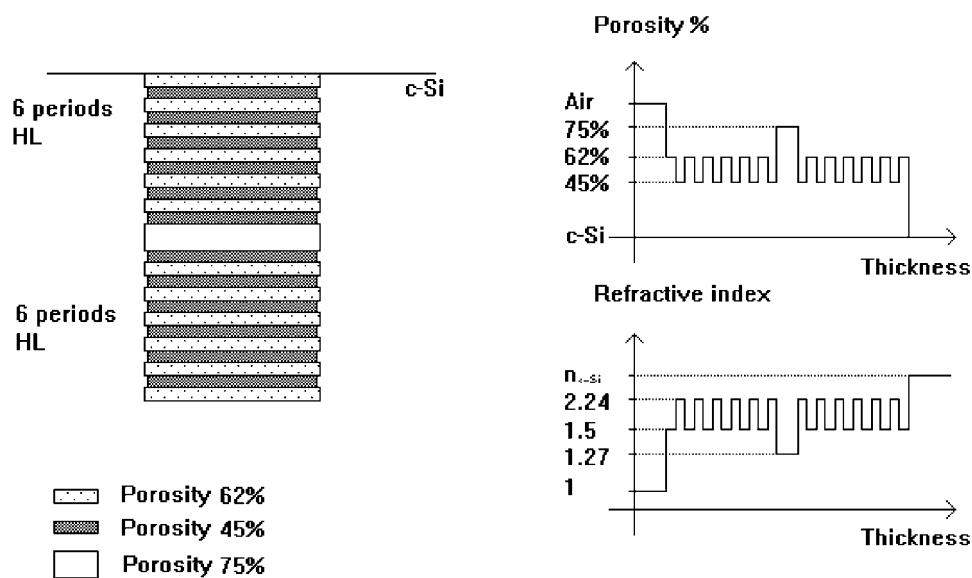


Figure 9. On the left, an illustration of a Fabry-Perot structure with 6 + 6 periods. On the right, the consequent porosity and index profile.

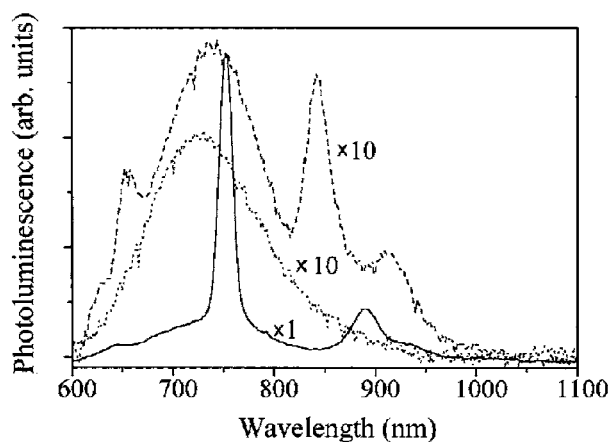


Figure 10. Room temperature PL spectra of the a PS microcavity PSM of thickness λ (solid curve), of a PS reference layer of thickness λ (dotted curve), and of a sample composed of 12 periods of PS layers each of thickness $\lambda/4$ with alternating porosities of 62 and 45% (dashed curve). The PL spectra were collected along the axis normal to the sample surface. In order to compare the various PL lineshapes, the emissions of the Bragg reflector and of the reference sample have been multiplied by a factor of 10.

Different substances affect different physical properties. This can be exploited to distinguish the substances parametrically. One of these sensitive properties is the electrical conductance between two electrodes on the surface of the PS layer. In figure 11 we show the response of PS in contact with air with a very low concentration of NO_2 . Also the PL depends sensitively on the surrounding gases. Polar molecules inside the structure quench the luminescence because the electric field created inside the pores due to the dipolar moment of

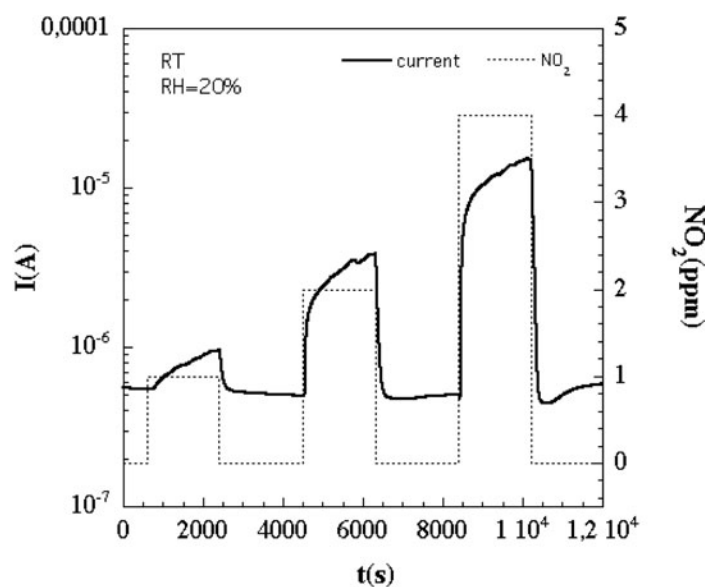


Figure 11. Electrical current through a low-resistivity PSM under a controlled flux (0.3 l m^{-1}) of humid air (20%) containing 1, 2, or 4 ppm of NO_2 .

the gas breaks the exciton. This allows measuring of the concentration of polar species, taking the integrated PL as the sensing parameter. Figure 12 shows an example of this dependence for different gases. Another physical parameter, which varies in the presence of different gases, is the effective refractive index n of PS, as the PL peak position (λ_c) of a microcavity depends on n as $\lambda_c = nd$, where d is the thickness of the central layer. λ_c is particularly dependent on the surroundings in which the microcavity is immersed. The narrowing of the PL peak in a microcavity allows the measuring of small variations of n , i.e. the detection of low gas concentrations. An example of a small shift in λ_c is shown in figure 13, where shifts of the order of 1–3 nm are detectable. Figure 14 shows another set of gases for which a clear trend is observed: the higher the gas refractive index, the larger the red-shift. Monitoring these three parameters at the same time allows estimation of the concentrations of different components of a mixture of gases. For example, it is worth noticing the fact that, as shown in figure 14, ethanol and pentane produce the same shift, but the PL quenching is much clearer for ethanol than for pentane (figure 12). Multiple parameters also lend robustness to the sensor, an important requirement for its efficacy. Other parameters could also be added to the set, such as the reflectance spectrum [96], waveguiding [97], and the electric response in frequency [98].

6.3. Light-emitting diodes

In order to implement use of PS in optoelectronic devices it is necessary to excite luminescence electrically (electroluminescence, EL) instead of optically (photoluminescence, PL). EL of PS was reported in 1991 soon after the discovery of PL [99]. The contacts were a metal plate in the back of the wafer and a HF-free solution as the front electrochemical contact. After the first demonstration of EL in PS, the challenge was to fabricate PS all-solid-state devices. The first results were obtained from $75 \mu\text{m}$ thick photoluminescent PS layers prepared on lightly doped n -type substrates [100]. The diodes were obtained from thin-film Au deposits.

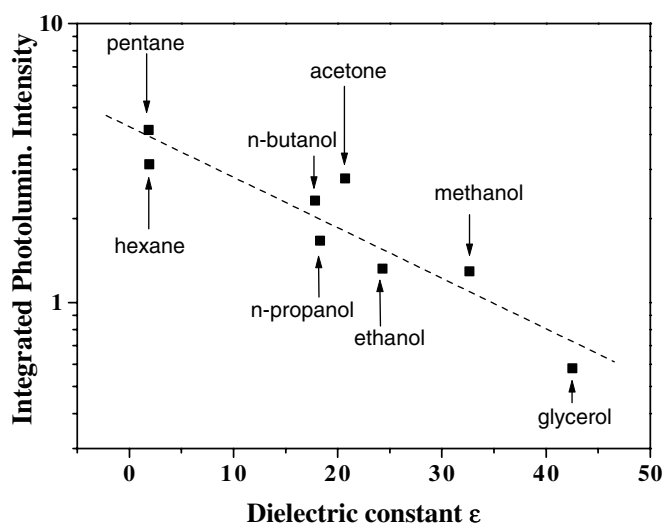


Figure 12. Integrated relative intensity (550–850 nm) as a function of the dielectric constant of the solvent for a PSM. The data are normalized with respect to the emission in air. The dashed line is only a guide for the eyes.

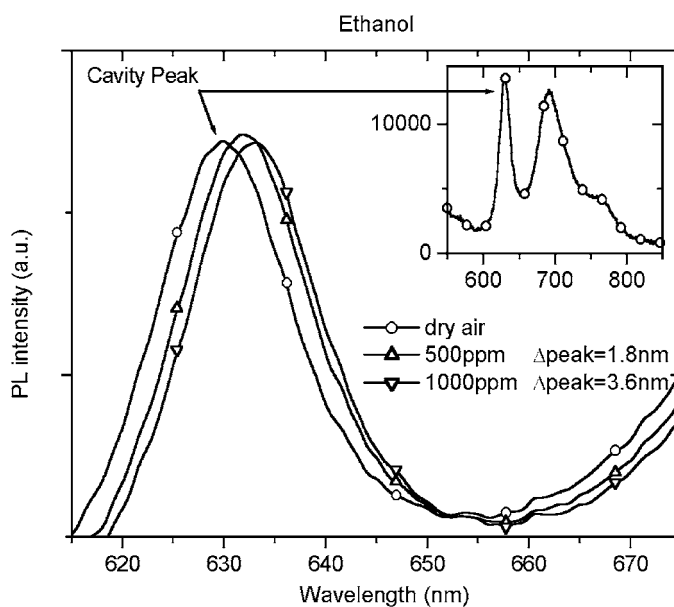


Figure 13. PL spectra of a high-resistivity PSM, under a controlled flux of air containing ethanol at room temperature. Spectra have been acquired 10 min after the switching on of the flux with the indicated concentration. Left plot: dry air (circles), dry air + ethanol (500 ppm: upward-pointing triangles; 1000 ppm: downward-pointing triangles).

The next step in LED development was the use of a true pn junction in 1992 [101]. A relatively good junction was obtained and the device showed a weak EL spectrum close to the PL spectrum. A typical turn-on voltage was 0.7 V, and EL was measured at 12.5 A cm^{-2} . The efficiency of these devices was low, but within this new approach the carrier injection

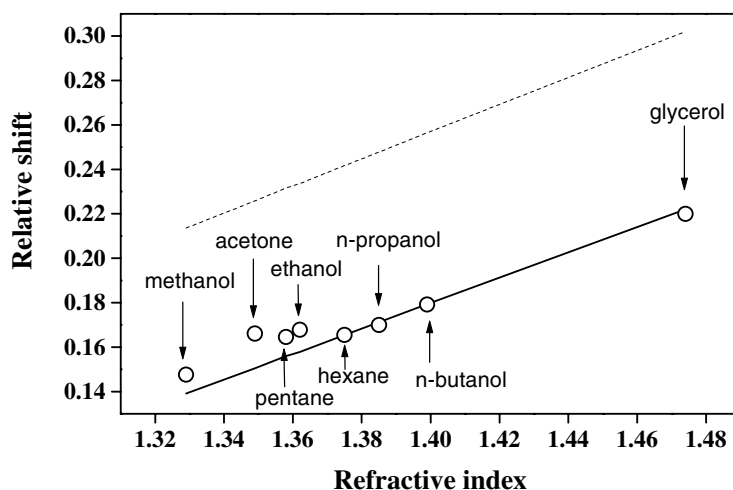


Figure 14. Relative peak shift versus refractive index for a PSM initially centred at 570 nm. Dashed line: calculated shift without inclusion of the variation of the PS refractive index with the wavelength. Solid line: calculated shift with this effect included. Open circles: experimental points.

mechanism was significantly improved, so high voltage was not required for excitation of the luminescence. Consequently other works have dealt with this kind of device [102, 103].

The first attempt to integrate a PS LED with Si electronics was carried out by integrating a bipolar transistor with a PS LED in 1996 [104]. The driving transistor, connected in the common-emitter configuration, modulated light emission by amplifying a small base input signal and controlling the current flow through the LED. With similar geometry, structures of various sizes were fabricated, with the active area ranging from 0.005 to 2 mm². It was possible to turn the LED on and off by applying a small current pulse to the base of the bipolar transistor. Arrays of such integrated structures have also been fabricated.

The most efficient PS-based LED so far were made by Gelloz and Koshida [105]. The external quantum efficiency achieved was greater than 1% and the power efficiency was 0.37%. The key step in producing these top-PS-performance LED was an electrochemical oxidation treatment, which allowed a gain of several orders of magnitude in efficiency to be achieved by considerably reducing the leakage current.

6.4. Macroporous Si as a photonic crystal

The rationale behind the use of PC in optoelectronic devices can be found elsewhere [106]. Si is a good candidate for use in developing PC and here we review the production of two-dimensional 2D PC in Si by anodic electrochemical dissolution. The electrochemical dissolution process has many advantages over other dry methods: it is simpler, cheaper, faster, technologically friendly, and wafer scalable.

The typical 2D PC that can be obtained with PS are constituted of air columns in a Si matrix. The air columns are the macropores, which are formed in Si when particular etching parameters are used. The formation of macropores in Si by anodic dissolution is a process optimized in the 1990s [107–109] and could be used to produce both pores and pillar lattices.

The dissolution mechanism for silicon in HF solution is quite complicated and not very well understood yet. The most widely accepted model [110] demands the presence on the surface of the semiconductor of holes, in this way F⁻ anions could cause a nucleophilic attack

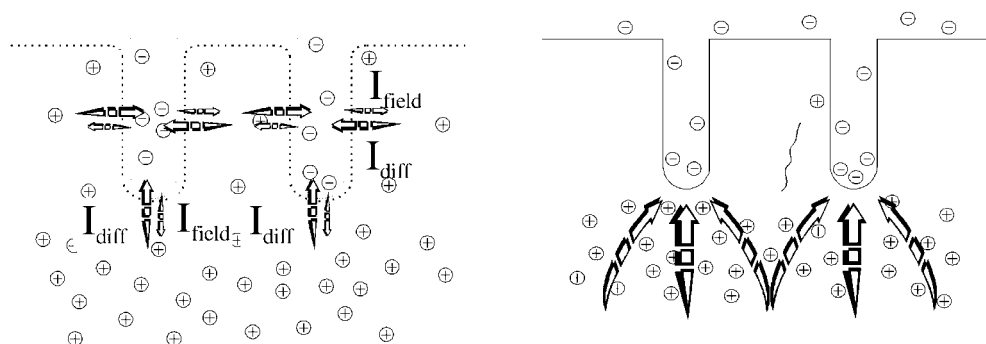


Figure 15. Left: the mechanism of dissolution for p-type silicon—highlighting the currents on the walls of the pores. Right: the mechanism for n-type silicon, in which all the carriers are collected and used for the dissolution at the bottom of the pores.

on the surface of the silicon and could break the bonds between silicon atoms. This model alone cannot explain the anisotropy of the Si dissolution. The anisotropy is determined by the electrical properties of the electrolyte/silicon junction, which is very different for p- and n-type-doped silicon [107, 108] (figure 15). In p-type-doped silicon the junction is forward biased. As usual in Schottky junctions, anodic currents due to the hole diffusion ($I_{diffusion}$) and the electric field (I_{field}) are present. The dissolution takes place everywhere where holes are present on the surface. An enhancement of the electric field occurs where the surface is curved, i.e. at the pore tips. Here the ratio $I_{field}/I_{diffusion}$ is greater and favours the dissolution at the pore tips over that at the pore walls. This means that on p-type silicon the electrochemical process produces pores that grow both in depth and laterally, but at two different rates. In n-type-doped Si the physics is different, because the junction resembles more a reverse-biased Schottky junction. Few holes are available for the dissolution reaction; thus by illuminating the back of the sample, more holes are generated in a region far from the electrolyte/Si interface. Photogenerated holes diffuse towards the surface, driven by the applied voltage, where the dissolution reaction takes place. Due to the large I_{field} , the pore tips collect most of the holes, impeding lateral growth of the pores. Because of this negligible lateral growth, n-type substrates are the most used for fabrication of PC.

The overall electrochemistry of the system is described by its $I-V$ characteristic. Figure 16 shows a typical curve where two current peaks are observed. The first is related to the threshold value for electropolishing, where the dissolution is homogeneous and the final surface has a mirror-like look. The second peak is connected with the formation of silicon oxide on the surface of the sample. Current values lower than the electropolishing threshold have to be used to form macropores.

To form 2D PC, one has to control the macropore surface arrangement. To periodically order the macropores on the surface, an initial lithographic step transfers to the surface the initial etch pit pattern. An attack in KOH develops the etch pits. Subsequently these etch pits are deepened with electrochemical dissolution. Thanks to the high anisotropy of the dissolution process, it is simple to reach a very high aspect ratio (radius of a pore divided by its length). The growth of the pores proceeds mainly along the (100) direction, but it is possible to induce growth in different directions by using oriented wafers and optimized electrolytes (figure 17) [111].

For p-type-doped Si, different geometries can be explored. Here we show some of our preliminary results on this. Different kinds of lattice can be obtained from a similar lithographic

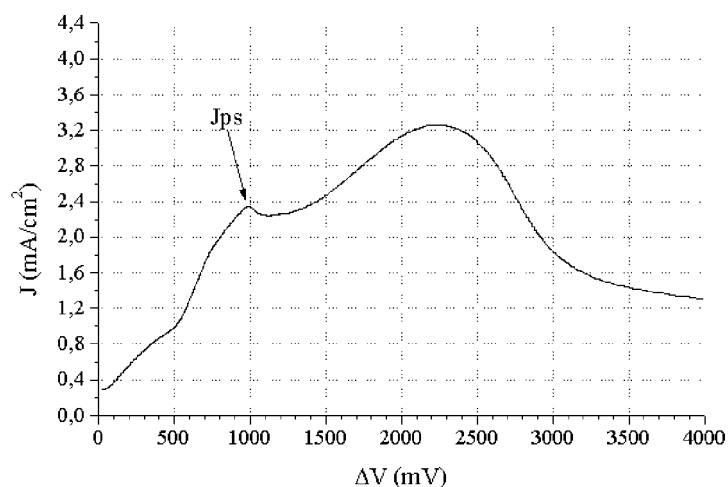


Figure 16. Voltammetry of an n-type silicon sample in 0.5 M HF. Scan rate: 50 mV s⁻¹.

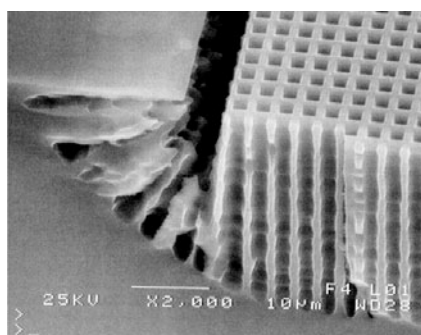


Figure 17. It is possible to induce growth of the pores in directions other than (100), but these pores are much less regular and less well controlled than the normal (100)-directed ones.

mask (figures 18 and 19). The initial mask had a square-lattice geometry where the pore diameters and spacing were different. On simply doubling the size of the lattice, a lattice with a double basis is obtained: a new pore forms in each interstitial position (figure 18). On decreasing the size of the lattice, a transition from a lattice of pores to a lattice of pillars is observed (figure 19). This is due to the lateral growth of the pores: the walls between adjacent pores are completely dissolved, leaving the Si columns at the wall crossings.

Once 2D PC are produced, they can also be infilled with active materials to form either enhanced LED or non-linear media. Some works report efforts along this route: from impregnation with quantum dots [112] to laser dyes [113,114] to Er ions [115,116]. We have impregnated our structure with Er ions by electromigration, where a macroporous sample is exposed to a saturated solution of Er chloride and, simply applying a cathodic bias to the sample, the Er ions are driven into the nanoporous layer that coats the pore walls. After impregnation, a thermal annealing is performed in air (10 min at 1200 °C). Figure 20 shows some preliminary results. A comparison with the luminescence of an Er-doped Si-nc produced by ion implantation is shown. The weaker PL intensity of the macroporous sample is due to the lower effective emitting area.

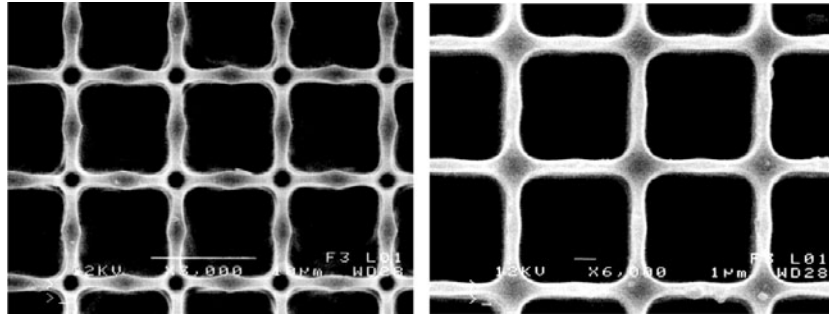


Figure 18. p-type silicon samples produced in HF 2.9 M, at 10 mA cm^{-2} for 40 min.

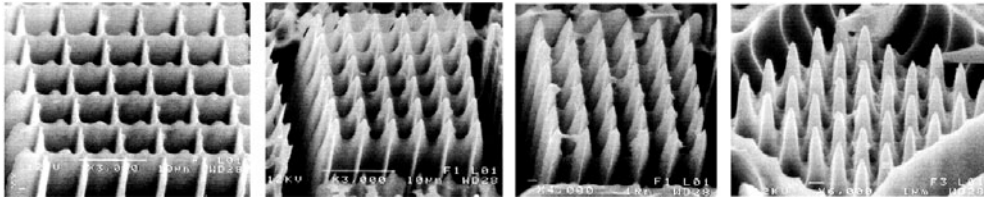


Figure 19. A progressive reduction of the lattice parameters produces, using the same etching conditions, a great effect on the final structure.

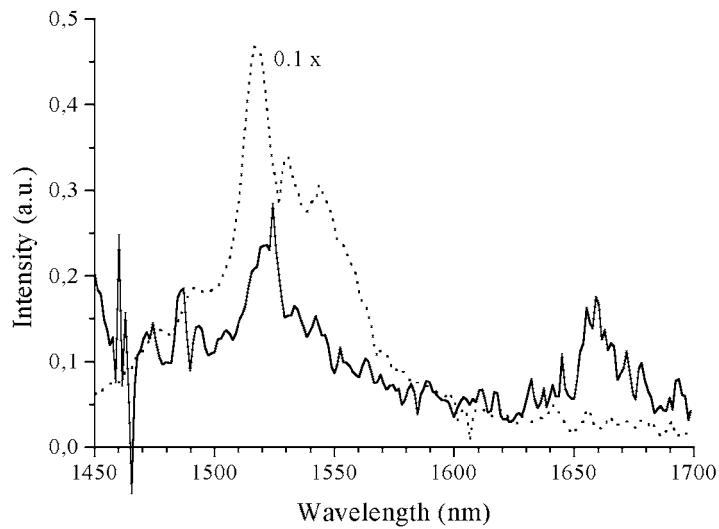


Figure 20. Luminescence from erbium-doped PS samples: solid curve: macroporous silicon sample; dotted curve: nanoporous sample. Note the different scales.

6.5. Porous Si Fibonacci quasicrystals

Anderson localization is a wave phenomenon that can be described as an effect of interference between counter-propagating waves. If the amount of disorder is high enough, a breakdown occurs in the diffusive wave transport, the diffusion constant vanishes, and the waves become localized. Localization of light waves in fully random three-dimensional systems has recently

been demonstrated for strongly scattering semiconductor powders [117]. In such systems the scattering mean free path becomes comparable with the wavelength of light, so a freely propagating wave can no longer build up over one oscillation of the electric field. For random one-dimensional systems, the scaling theory of localization [118] predicts that all the states are exponentially localized for any arbitrary degree of disorder. There will be no diffusive transport along the direction of disorder and the usual random-walk picture will be completely invalidated by interference effects. A similar picture holds for light propagation in one-dimensional aperiodic structures [119–121]. Deterministic aperiodic structures are obtained by the iteration of some deterministic prescription, called the generating rule, but are characterized by the lack of any translational periodicity. One class of deterministic aperiodic structures is represented by the Fibonacci quasicrystals [122–124]: multilayer structures constructed recursively as $S_{j+1} = \{S_{j-1}S_j\}$ for $j \geq 1$, where $S_0 = \{B\}$ and $S_1 = \{A\}$. In this sequence, $S_2 = \{BA\}$, $S_3 = \{ABA\}$, $S_4 = \{BAABA\}$, $S_5 = \{ABABAABA\}$, and so on. Of particular interest is the possibility of addressing experimentally the question of light transport and localization in deterministic aperiodic structures, where the diffusion characteristics are strongly affected by the aperiodicity of the system on one hand, and by the structure irregularities and random unavoidable perturbations on the other.

Here we report the band-edge pulse propagation of PS Fibonacci quasicrystals, where the most dramatic effects are expected. To address this question, we have grown electrochemically a Fibonacci quasicrystal with $j = 12$ (up to 233 layers) starting from a p^+ -type-doped Si wafer. S_0 was an 165 nm thick layer with 66% porosity and S_1 was an 110 nm thick layer with 45% porosity. The total thickness of the 233-layer sample was approximately 30 μm .

Figure 21 reports the band-edge transmission spectrum of the Fibonacci structure together with a transfer-matrix simulation. To obtain good agreement with the experiments, the simulation included a small linear drift both in the layer thickness and in the porosity (see section 3). The thickness of S_0 was varied linearly up to a maximum of 4% of its initial value; that of S_1 was varied linearly by less than 1% over the entire structure, while their porosities were varied by up to 6% of their initial values. A different kind of correction arises from the unavoidable lateral inhomogeneities, which turned out to be less than 1% of the nominal value. Taking into account these corrections, it is possible to obtain a good agreement with the measured transmission spectrum of the structure only in the frequency region below 5500 cm^{-1} , where the absorption of the Si substrate and that of PS itself are negligible.

We focused our attention on just a narrow region of about 500 cm^{-1} at the band edge, where the time dynamics of femtosecond laser pulses transmitted through the Fibonacci samples and spanning in frequencies the entire band edge has been studied by means of phase-sensitive interferometric techniques [125]. In figure 22 we show some of the input Gaussian laser pulses that are in resonance with the band edge, together with the measured and calculated time responses of the structure. The transmitted pulse lineshapes depend on the energy of the pulses. When the pulse energy is resonant with only a single optical mode (the single transmission peak in figure 22, top), the pulse is significantly delayed and exponentially stretched (see e.g. figure 22, curve 4). In addition to the delay and stretching, when the pulse energy overlaps with two narrow transmission modes (see e.g. figure 22, curve 3), a coherent beating of these different modes is observed whose oscillation frequency corresponds to the frequency difference between the excited optical modes.

The pulse delay is due to both the band-gap effect and the localized character of the band-edge mode that has been excited. It is well known [126] that even in perfectly ordered and periodic structures localized modes, called band-edge resonances, can appear at the band edge. These modes are extremely narrow and are characterized by an enhancement of the electromagnetic field. The field enhancement is due to the interplay of a quasi-

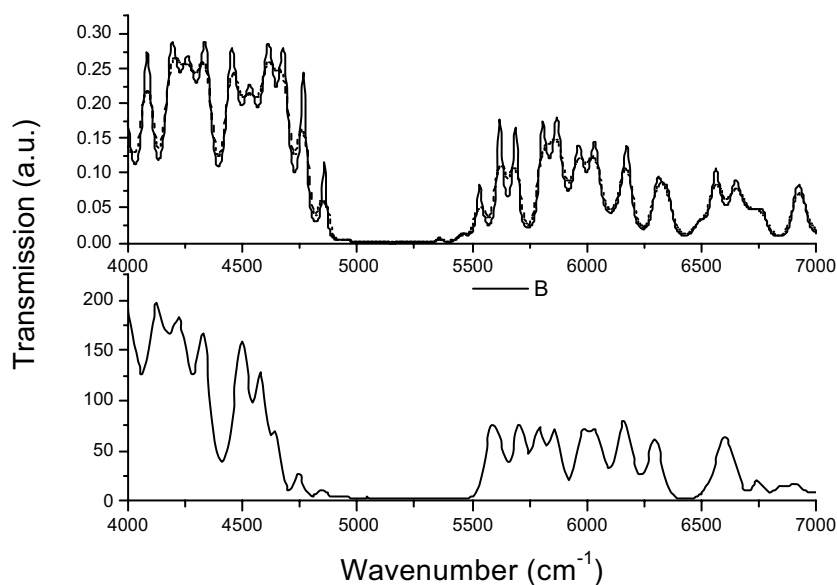


Figure 21. Upper plots: transfer-matrix simulations of the transmission spectrum of the Fibonacci quasicrystals. Solid curve: simulation of the uniform structure. Dashed curve: simulation of the transmission spectrum considering a 1% lateral inhomogeneity of the layer thicknesses. The absorption of the silicon substrate (as well as that of the PS layers) has been included in both simulations. Lower plot: the experimental transmission spectrum for the Fibonacci quasicrystals.

standing wave, transiently formed inside the layered structure, and the forward-propagating electromagnetic field of the propagating pulse. Within this simplified physical picture, energy is scattered from the forward-propagating fields into the quasi-standing wave, and back into the forward-propagating fields. The wave oscillates inside the crystal and can transiently store a substantial amount of electromagnetic energy. This effect is manifested in our experiment by the substantial stretching of the pulse. The resonant excitation of two adjacent narrow transmission modes produces the observed coherent beating in the time domain. For incident pulses far away from the band edge, no such effects have been measured.

To further clarify the nature of the transmission band-edge states, we have calculated the field distribution of the optical modes inside the structure. The results of the calculations are shown in figure 23. In the frequency region between 4750 and 4850 cm^{-1} , the field amplitude distributions do not show Bloch-like behaviours, but do have localized nature. The electric field intensity of these modes shows a small field-enhancement effect, i.e. the field intensity inside the sample is locally greater than the intensity of the incident pulse. The field enhancement in the Fibonacci sample is not as dramatic as one would expect for fully disordered systems, because the modes of the Fibonacci sample are weakly localized and not exponentially localized. Their nature is somewhere in between that of exponentially localized states and that of extended Bloch states.

To our knowledge this is the first demonstration of the presence of localized photon states from time-resolved propagation measurements in Fibonacci quasicrystals.

7. Conclusions

Initiated by technical investigations in the 1940s, and started as an industry in the late 1960s, planar Si technology has distinguished itself by the rapid improvements in its products. While

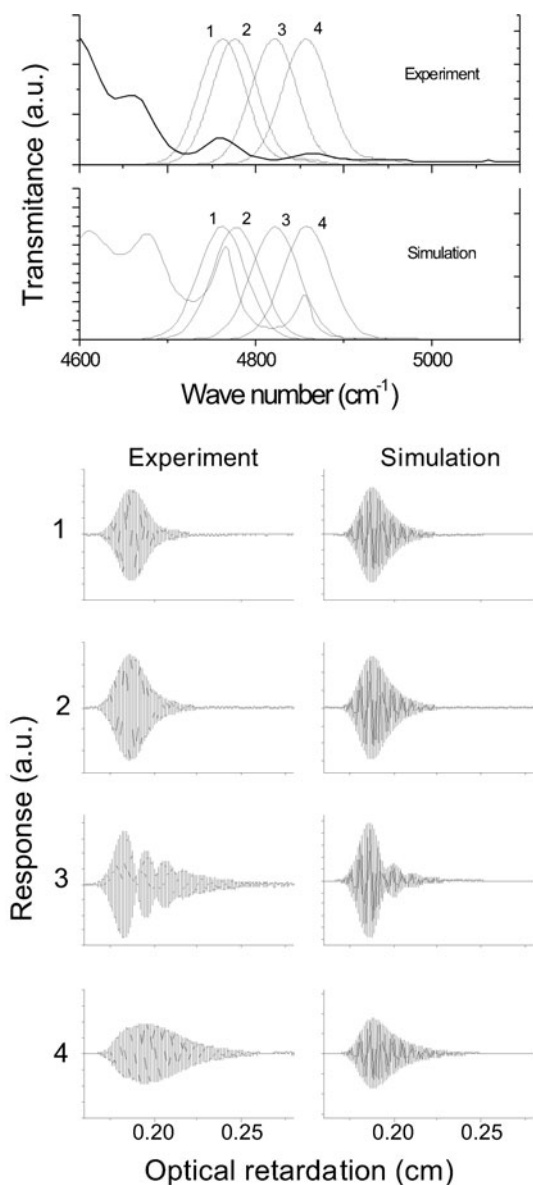


Figure 22. Upper plots: measured band-edge and input laser profiles ('experiment'); simulations of the sample band edge with incident Gaussian laser pulses ('simulation'). Lower plots: measured ('experiment') and simulated ('simulation') time responses of the sample corresponding to the different pulses indicated by the numbers in the figure.

the indirect nature of its band gap, on one hand, and the satisfactory performance of CMOS electronic devices, on the other, postponed any significant investment in Si photonics up to the 1990s, we believe now that the prospects for exploiting Si photonics are no longer poor. On the materials side, the rapidly growing nanotechnology has shown that the optical properties of bulk crystalline materials can be dramatically changed by shrinking their sizes. On the applications side, we have witnessed a number of intriguing discoveries related to the interaction between light and matter, such as quasicrystals and PBG. Simultaneously, the integration level and

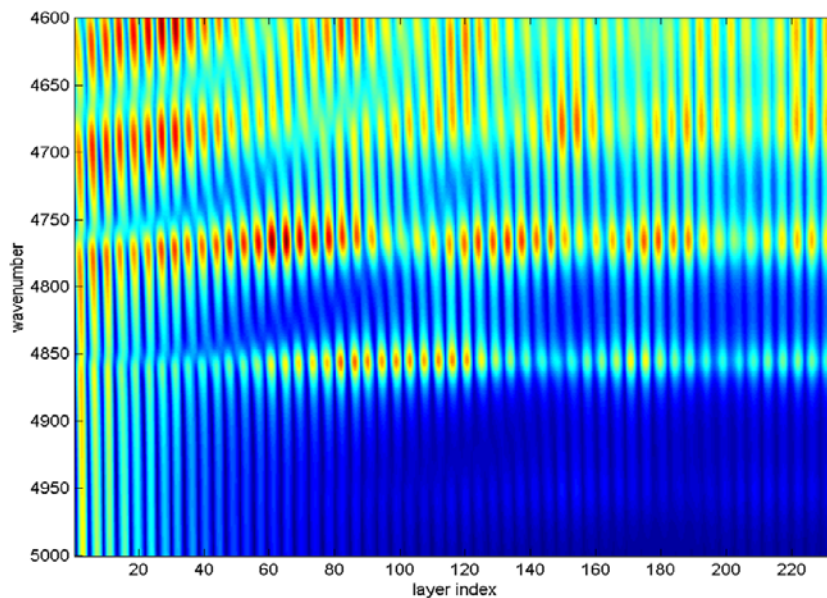


Figure 23. The scattering state calculation of the field intensity distribution inside the Fibonacci structure.

interconnect bandwidth requirements are pushing harder towards the introduction of optical functionality inside integrated circuits.

In the last decade, Si LED and optoelectronic devices, optical gain in Si nanocrystals, and Si photonic band-gap materials have been demonstrated. Many such achievements were first observed in nanoporous or in macroporous Si, whose fabrication is very inexpensive. At present, PS is difficult to control, in particular as regards its growth and its stability over time. It is hard to predict whether it will be possible to control the stability to the degree required by the applications. Even though it might be necessary to employ different—and certainly more expensive—procedures for Si nanocrystal fabrication, the availability of PS is a fortunate circumstance, to demonstrate the feasibility for Si-based photonics. The race is now on to achieve all-Si-based integrated photonic circuits.

Acknowledgments

The work reported here is the outcome of numerous collaborations.

On silicon nanocrystals: with the groups of Professor Priolo of INFN and the University of Catania and of Dr Iacona at IMETEM-CNR. It has been carried out in the framework of the special project LUNA and the advanced research project RAMSES of INFN. It has also been supported by MURST through the programme COFIN99 coordinated by S Modesti.

On photonic crystals: with the Microsystem Division of ITC-irst, and with the groups of Professor Andreani and Professor Marabelli of INFN and the University of Pavia. It was supported by MURST through the programme COFIN00 coordinated by L C Andreani. The fine SEM photographs were taken by A Lui, who we thank.

On Fibonacci quasicrystals: with the 'waves in complex media' group of Professor Ad Lagendijk at the Van der Waals–Zeeman Institute of Amsterdam and with Dr D Wiersma at the LENS in Florence. It has been supported by the University of Trento through the programme Giovani Ricercatori MARC and by INFN through the project RANDLAS.

On porous silicon sensors: with Professors Sberveglieri and Faglia of the University of Brescia, and financed by INFM through the project SMOG and by PAT through a project coordinated by Professor G Soncini.

On porous Si LED: with P Bellutti, and supported by CNR through the project MADESS. Among others, we wish to thank S Ossicini for fruitful discussions and theoretical support.

References

- [1] *International Technology Roadmap for Semiconductors, 2000 Update, Interconnect* (Electronic Document at the International SEMATECH Internet web site <http://public.itrs.net>)
- [2] Bisi O, Campisano S U, Pavesi L and Priolo F (ed) 1999 *Silicon Based Microphotonics: from Basics to Applications* (Amsterdam: IOS press)
- [3] Gelloz B and Koshida N 2000 *J. Appl. Phys.* **88** 4319
- [4] Green M A, Zhao J, Wang A, Reece P J and Gal M 2001 *Nature* **412** 805
- [5] Pavesi L, Dal Negro L, Mazzoleni C, Franzò G and Priolo F 2000 *Nature* **408** 440
- [6] Bisi O, Ossicini S and Pavesi L 2000 *Surf. Sci. Rep.* **264** 1
- [7] Linnros I 1999 *Silicon Based Microphotonics: from Basics to Applications* (Amsterdam: IOS press) p 47
- [8] Iacona F, Franzò G and Spinella C 2000 *J. Appl. Phys.* **87** 1295
- [9] Dinh L N, Chase L L, Balooch M, Terminello L and Wooten F 1994 *Appl. Phys. Lett.* **65** 3111
- [10] Lu Z H, Lockwood D J and Baribeau M 1995 *Nature* **378** 258
- [11] Baribeau J M, Lockwood D J, Lu Z H, Labbe H J, Rolfe S J and Sproule G L 1999 *J. Lumin.* **80** 417
- [12] Morisaki H, Ping F W, Ono H and Yazawa K J 1991 *Appl. Phys. Lett.* **70** 1869
- [13] Canham L T 1990 *Appl. Phys. Lett.* **57** 1045
- [14] Ulhir A 1956 *Bell Syst. Tech. J.* **35** 333
- [15] Pavesi L 1997 *Nuovo Cimento* **20** 1
- [16] Lehmann V and Grunin U 1997 *Thin Solid Films* **297** 13
- [17] Yablonovitch E 1987 *Phys. Rev. Lett.* **58** 2059
- [18] Dal Negro L *et al* 2002 at press
- [19] Anderson P W 1958 *Phys. Rev.* **109** 1942
- [20] Pickering C, Beale M I J, Robbins D J, Pearson P J and Greef R 1984 *J. Phys. C: Solid State Phys.* **17** 6535
- [21] Theiß W 1997 *Surf. Sci. Rep.* **29** 91
- [22] Thönissen M, Billat S, Krüger M, Lüth H, Berger M G, Frotscher U and Rossow U 1996 *J. Appl. Phys.* **80** 2990
- [23] Manotas S, Agulló-Rueda F, Moreno J D, Martín-Palma R J, Guerrero-Lemus R and Martínez-Duart J M 1999 *Appl. Phys. Lett.* **75** 977
- [24] Pickering C, Canham L T and Brumhead D 1993 *Appl. Surf. Sci.* **63** 22
- [25] Faivre C, Bellet D and Dolino G 1999 *Eur. Phys. J.* **B 7** 19
- [26] Thönissen M *et al* 1997 *Thin Solid Films* **297** 92
- [27] Gaburro Z, Oton C J, Bettotti P, Dal Negro L, Vijaya Prakash G, Cazzanelli M and Pavesi L 2002 *J. Electrochem. Soc.* submitted
- Pavesi L, Gaburro Z, Dal Negro L, Bettotti P, Vijaya Prakash G J, Cazzanelli M and Oton C 2002 *Optics and Laser Engineering* **38** 81
- [28] Vijaya Prakash G *et al* 2001 *J. Nanosci. Nanotechnol.* **1** 159
- [29] Priolo F, Franzò G, Pacifici D, Vinciguerra V, Iacona F and Irrera A 2001 *J. Appl. Phys.* **89** 264
- [30] Shimizu-Iwayama T, Fujita K, Nakao S, Saitoh K, Fujita T and Itoh N 1994 *J. Appl. Phys.* **75** 7779
- [31] Dinh L N, Chase L L, Balooch M, Terminello L J and Wooten F 1994 *Appl. Phys. Lett.* **65** 1824
- [32] Dinh L N, Chase L L, Balooch M, Siekhaus W J and Wooten F 1996 *Phys. Rev. B* **54** 5029
- [33] Hill N A and Whaley K B 1995 *Phys. Rev. Lett.* **75** 1514
- [34] Shiba K, Nakagawa K, Ikeda M, Kohno A, Miyazaki S and Hirose M 1997 *Japan. J. Appl. Phys.* **36** 1279
- [35] Ma Z, Liao X, He J, Cheng W, Yue G, Wang Y and Kong G 1998 *J. Appl. Phys.* **83** 7934
- [36] Cheylan S and Elliman R G 2001 *Appl. Phys. Lett.* **78** 1912
- [37] Fujii M, Mimura A, Hayashi S, Yamamoto K, Urakawa C and Ohta H 1999 *Appl. Phys. Lett.* **75** 184
- [38] Henari F Z, Morgenstern K, Blau W J, Karavanski V A and Dneprovskii V S 1995 *Appl. Phys. Lett.* **67** 323
- [39] Lettieri S, Maddalena P, Odierna L P, Ninno D, La Ferrara V and Di Francia G 2001 *Phil. Mag.* **B 81** 133
- [40] Vijaya Lakshmi S, Shen F and Grebel H 1997 *Appl. Phys. Lett.* **71** 3332
- [41] Vijaya Lakshmi S, George M A and Grebel H 1997 *Appl. Phys. Lett.* **70** 708

- [42] Borsella E, Falconieri M, Botti S, Martelli S, Bignoli F, Costa L, Grandi S, Sangaletti L, Allieri B and Depero L 2001 *Mater. Sci. Eng. B* **79** 55
- [43] Vijaya Prakash G, Cazzanelli M, Gaburro Z, Pavesi L, Iacona F, Franzò G and Priolo F 2002 *J. Mod. Opt.* at press
- [44] Sheik-Bahae M, Said A A and Van Stryland E W 1989 *Opt. Lett.* **14** 955
- [45] Vogel E M, Weber M J and Krol D M 1991 *Phys. Chem. Glasses* **32** 231
- [46] Reitze D H, Zang T R, Wood W M and Downer M C 2000 *J. Opt. Soc. Am. B* **7** 84
- [47] Reintjes J F and McGroddy J C 1973 *Phys. Rev. Lett.* **30** 901
- [48] Vijaya Lakshmi S, Grebel H, Iqbal Z and White C W 1998 *J. Appl. Phys.* **84** 6502
- [49] Vijaya Lakshmi S, Grebel H, Yaglioglu G, Pino R, Dorsinville R and White C W 2000 *J. Appl. Phys.* **88** 6418
- [50] Shen Y R 1984 *The Principles of Nonlinear Optics* (New York: Wiley) p 202
- [51] Wynne J J 1969 *Phys. Rev.* **178** 1295
- [52] Murayama M and Nakayama T 1994 *Phys. Rev. B* **49** 5737
Murayama M and Nakayama T 1995 *Phys. Rev. B* **52** 4986
- [53] Ballesteros J M, Solis J, Serna R and Afonso C N 1999 *Appl. Phys. Lett.* **74** 2791
- [54] Lettieri S, Fiore O, Maddalena P, Ninno D, Di Francia G and La Ferrara V 1999 *Opt. Commun.* **168** 383
- [55] Schmitt-Rink S, Miller D A B and Chemla D S 1987 *Phys. Rev. B* **35** 8113
- [56] Hanamura E 1988 *Phys. Rev. B* **37** 1273
- [57] Cotter D, Burt M G and Manning R J 1992 *Phys. Rev. Lett.* **68** 1200
- [58] Chen R, Lin D L and Mendoza B 1993 *Phys. Rev. B* **48** 11 879
- [59] Pavesi L, Dal Negro L, Mazzoleni C, Franzò G and Priolo F 2000 *Nature* **408** 440
- [60] Shaklee K L, Nahaory R E and Leheny R F 1973 *J. Lumin.* **7** 284
Hvam J M 1978 *J. Appl. Phys.* **49** 3124
- [61] Jordan V 1994 *IEEE Proc. Optoelectron.* **141** 13
- [62] Yariv A 1974 *Quantum Electronics* 2nd edn (New York: Wiley)
- [63] Saleh B E A and Teich M C 1991 *Fundamentals of Photonics* (New York: Wiley)
- [64] Dumke W P 1962 *Phys. Rev.* **127** 1559
- [65] Wolkin M V, Jorne J, Fauchet P M, Allan G and Delerue C 1999 *Phys. Rev. Lett.* **82** 197
- [66] Allan G, Delerue C and Lannoo M 1996 *Phys. Rev. Lett.* **76** 2961
- [67] Kobitski A Y, Zhuravlev K S, Wagner H P and Zahn D R T 2001 *Phys. Rev. B* **63** 115423
- [68] Coffa S, Libertino S, Coppola G and Tutolo A 2000 *IEEE J. Quantum Electron.* **36** 1206
- [69] Palm J, Gan F, Zheng B, Mitchel J and Kimerling L C 1996 *Phys. Rev. B* **54** 17 602
- [70] Priolo F, Franzò G, Coffa S, Polman A and Carnera A 1998 *Phys. Rev. B* **57** 4443
- [71] Franzò G, Priolo F, Coffa S, Polman A and Carnera A 1994 *Appl. Phys. Lett.* **64** 2235
- [72] Zheng B, Michel J, Ren F Y G, Kimerling L C, Jacobson D C and Poate J M 1994 *Appl. Phys. Lett.* **64** 2842
- [73] Kimerling L C 1997 *Quarterly Status Report for USAF Rome Laboratory, Contract F19628-95-C-0049*, October
- [74] Kenyon A J, Trwoga P F, Federighi M and Pitt C W 1994 *J. Phys.: Condens. Matter* **6** L319
- [75] Franzò G, Iacona F, Vinciguerra V and Priolo F 1999 *Mater. Sci. Eng. B* **69+70** 338
- [76] Chan S and Fauchet P M 1999 *Appl. Phys. Lett.* **75** 274
- [77] Friedman L, Soref R A and Sun G 1998 *J. Appl. Phys.* **83** 3480
- [78] Sun G, Lu Y and Khurgin J B 1998 *Appl. Phys. Lett.* **72** 1481
- [79] Friedman L, Sun G and Soref R A 2001 *Appl. Phys. Lett.* **78** 401
- [80] Dehlinger G, Diehl L, Gennser U, Sigg H, Faist J, Ensslin K, Grützmacher and Müller E 2000 *Science* **290** 2277
- [81] Heikkilä L, Kuusela T and Hedman H P 1999 *Superlatt. Microstruct.* **26** 157
- [82] Khriachtchev L, Räsänen M, Novikov S and Sinkkonen J 2001 *Appl. Phys. Lett.* **79** 1249
- [83] Nayfeh M H, Therrien J, Belomoin G, Akcakir O, Barry N and Gratton E 2001 *Mater. Res. Soc. Symp. Proc.* **638**
- [84] Born M and Wolf E 1980 *Principles of Optics* (Oxford: Pergamon)
- [85] Mulloni V, Mazzoleni C and Pavesi L 1999 *Semicond. Sci. Technol.* **14** 1052
- [86] Krüger M, Hilbrich S, Thönissen M, Scheyen D, Theiß W and Lüth H 1998 *Opt. Commun.* **146** 309
- [87] Mulloni V and Pavesi L 2000 *Mater. Sci. Eng. B* **69+70** 59
- [88] Araki M, Koyama H and Koshida N 1996 *Appl. Phys. Lett.* **68** 2999
- [89] Mulloni V and Pavesi L 2000 *Appl. Phys. Lett.* **76** 2523
- [90] Harper J and Sailor M J 1996 *Anal. Chem.* **68** 3713
- [91] Baratto C, Faglia G, Sberveglieri G, Boarino L, Rossi A M and Amato G 2001 *Thin Solid Films* **391** 261
- [92] Mares J J, Kristofik J and Hulicius E 1995 *Thin Solid Films* **255** 272

- [93] Foucaran A, Sorli B, Garcia M, Pascal-Delannoy F, Giani A and Boyer A 2000 *Sensors Actuators A* **79** 189
- [94] Gaburro Z, Daldosso N, Pavesi L, Faglia G, Baratto C and Sberveglieri G 2001 *Appl. Phys. Lett.* **78** 3744
- [95] Chan S, Fauchet P M, Li Y, Rothberg L J and Miller B L 2000 *Phys. Status Solidi a* **182** 541
- [96] Snow P A, Squire E K, Russel P S J and Canham L T 1999 *J. Appl. Phys.* **86** 1781
- [97] Arrand H F, Benson T M, Loni A, Arens-Fischer R, Krüger M G, Thönissen M, Lüth H, Kershaw S and Vorozov N N 1998 *J. Lumin.* **80** 119
- [98] Motohashi A, Kawakami M, Aoyagi H, Kinoshita A and Satou A 1995 *Japan. J. Appl. Phys.* **34** 5840
- [99] Halimaoui A, Oules C, Bomchil G, Bsiesy A, Gaspard F, Herino R, Ligeon M and Muller F 1991 *Appl. Phys. Lett.* **59** 304
- [100] Richter A, Steiner P, Kozlowski F and Lang W 1991 *IEEE Electron. Device Lett.* **12** 691
- [101] Bassous E, Freeman M, Halbout J M, Iyer S S, Kesan V P, Munguia P and Williams B L 1992 *Mater. Res. Soc. Symp. Proc.* **256** 23
- [102] Tsybeskov L, Duttagupta S P, Hirschmann K D and Fauchet P M 1996 *Appl. Phys. Lett.* **68** 2058
- [103] Pavesi L, Guardini R and Bellutti P 1997 *Thin Solid Films* **297** 272
- [104] Hirschmann K D, Tsybeskov L, Duttagupta S P and Fauchet P M 1996 *Nature* **384** 338
- [105] Gelloz B and Koshida N 2000 *J. Appl. Phys.* **88** 4319
- [106] Weisbuch C, Benisty H, Olivier S, Rattier M, Smith C J M and Krauss T F 2000 *Phys. Status Solidi b* **221** 93
- [107] Lehmann V and Föll H 1990 *J. Electrochem. Soc.* **137** 653
- [108] Lehmann V and Rönnebeck S 1999 *J. Electrochem. Soc.* **146** 2968
- [109] Lehmann V 1993 *J. Electrochem. Soc.* **140** 2836
- [110] Lehmann V and Gösele U 1991 *Appl. Phys. Lett.* **58** 856
- [111] Christophersen M, Carstensen J and Föll H 2000 *Phys. Status Solidi a* **182** 103
- [112] Yoshie T, Scherer A, Chen H, Huffaker D and Deppe D 2001 *Appl. Phys. Lett.* **79** 114
- [113] Schriemer H P, van Driel H M, Koenderink A F and Vos W L 2001 *Phys. Rev. A* **63** 01180R
- [114] Yoshino K, Tatsuhara S, Kawagishi Y, Ozaki M, Zakhidov A A and Vardeny Z V 1999 *Appl. Phys. Lett.* **74** 2590
- [115] Rimura T, Yokoi A, Horiguchi H, Saito R, Ikoma T and Sato A 1994 *Appl. Phys. Lett.* **65** 983
- [116] Lopez H A and Fauchet P M 1999 *Appl. Phys. Lett.* **75** 3989
- [117] Wiersma D S, Bartolini P, Lagendijk A and Righini R 1997 *Nature* **390** 671
- [118] Ping Sheng 1995 *Introduction to Wave Scattering, Localization, and Mesoscopic Phenomena* (New York: Academic)
- [119] Gellermann W, Kohmoto M, Sutherland B and Taylor P C 1994 *Phys. Rev. Lett.* **72** 633
- [120] Kohmoto M, Sutherland B and Iguchi K 1987 *Phys. Rev. Lett.* **58** 2436
- [121] Peng R W, Wang M, Hu A, Jiang S S, Gin G J and Feng D 1998 *Phys. Rev. B* **57** 1544
- [122] Kohmoto M and Sutherland B 1987 *Phys. Rev. B* **35** 1020
- [123] Desideri J P, Macon L and Sornette D 1989 *Phys. Rev. Lett.* **63** 390
- [124] Capaz R B, Koiller B and Queiroz S L A 1990 *Phys. Rev. B* **42** 6402
- [125] Rik H, Kop J and Sprik R 1995 *Rev. Sci. Instrum.* **66** 5459
- [126] Scalora M *et al* 1996 *Phys. Rev. E* **54** 1078